# PNAS

## www.pnas.org

**Supplementary Information for**

Dual-field-of-view high-spectral-resolution lidar: simultaneous profiling of aerosol and water cloud to study aerosol-cloud interaction

Nanchao Wang[a,†], Kai Zhang[a,†], Xue Shen[a,†], Yuan Wang[b], Jing Li[c], Chengcai Li[c], Jietai Mao[c], Aleksey Malinka[d], Chuanfeng Zhao[e], Lynn M. Russell[f], Jianping Guo[g], Silke Gross[h], Chong Liu[a,i], Jing Yang[a], Feitong Chen[a], Lingyun Wu[a], Sijie Chen[a], Ju Ke[a], Da Xiao[a], Yudi Zhou[a], Jing Fang[a], and Dong Liu[a,i,*]

[a]State Key Laboratory of Modern Optical Instrumentation, College of Optical Science and Engineering, Zhejiang University, Hangzhou 310000; [b]Division of Geological and Planetary Sciences, California Institute of Technology, Pasadena, CA 91109; [c]Department of Atmospheric and Oceanic Sciences, Laboratory for Climate and Ocean-Atmosphere Studies, School of Physics, Peking University, Beijing 100871; [d]Institute of Physics, National Academy of Sciences of Belarus, Minsk 220072; [e]State Key Laboratory of Earth Surface Processes and Resource Ecology, College of Global Change and Earth System Science, Beijing Normal University, Beijing 100088; [f]Scripps Institution of Oceanography, University of California, San Diego, CA 92093; [g]State Key Laboratory of Severe Weather, Chinese Academy of Meteorological Sciences, Beijing 100081; [h]Institut für Physik der Atmosphäre, Deutsches Zentrum für Luft und Raumfahrt, Oberpfaffenhofen 74397; [i]International Research Center for Advanced Photonics, Zhejiang University, Hangzhou 310000

[†]These authors contributed equally to this work.
[*]Corresponding author: Dong Liu. **Email:** liudongopt@zju.edu.cn

**This PDF file includes:**

> Text S1 to S6 (Text S1 through S7 are referenced in the main manuscript)
> Figures S1 to S12 (Figure S1-S7 and S9 are referenced in the main manuscript)
> Tables S1 to S3 (Tables S1 through S3 are referenced in the main manuscript)
> SI References

**Supplementary Information Text**

**S1. Description of dual-field-of-view(FOV) high-spectral-resolution lidar (HSRL) system.**

The transmitting laser is a diode pumped, Q-switched, injection seeded, frequency doubled Nd: YAG laser. A Glan-Taylor prism, which can only divert the ordinary polarization component of the incident light, is employed to ensure high polarization purity of the laser output. Then a small fraction of the transmitted light and received light is picked off into a power meter and a camera to monitor current laser output power and the alignment of the receiver, respectively. The backscattered photons, which contain the height-resolved atmospheric information, are collected using two vertically mounted telescopes with different FOVs independently. Receiver-I with narrow-FOV consists of a polarization beam splitter (PBS) and a beam splitter (BS) to separate the backscattering signals into three channels: combined perpendicular channel, combined parallel channel, and molecular channel. Two combined channels for perpendicular and parallel polarization components respectively receive the photons of both aerosol and molecular backscattering, whereas only the molecular scattering is detected by the molecular channel. Thus, the depolarization ratio, backscattering, and extinction can be retrieved from these three channels. These observations contribute to identifying the type of aerosols and the thermodynamic phase of clouds, which benefit the aerosol-cloud interaction (ACI) analysis. Receiver-II with wide-FOV consists of a molecular channel to simultaneously provide extinction observations with different receiver FOVs. Both molecular channels of two receivers equip with the iodine vapor cell to eliminate the particulate backscattering and pass the molecular backscattering (1).

**S2. Data processing scheme of dual-FOV HSRL to study ACI.**

The procedure of the data processing of dual-FOV HSRL is organized as followed (see *SI* Fig. S1). In the first step, the original lidar profiles, calibration constants, as well as meteorological data are used as the basic inputs for the pre-processing, such as background noise subtraction. After the pre-processing, the following operations are done on the signals to improve the signal-to-noise ratio (SNR): temporal averaging over a time window, and spatial filtering; then signal corrections, including gain correction, range correction, and overlap correction, are applied to generate the corrected lidar profiles. These corrected lidar profiles are employed to determine the vertical extent of aerosols and clouds (i.e., feature detection). To analyze the properties of aerosols and clouds respectively, the height range of the clouds is identified and separated from that of the aerosols, which was also referred to as cloud-aerosol discrimination (2). Then the corrected attenuated backscattering signals, available with the resolution of 5 min and 7.5 m, are used to retrieve the basic optical properties via numerical computation (3). The corrected attenuated backscattering signals of three channels can be expressed as

$$B_C^{\perp} = (\beta_m^{\perp} + \beta_p^{\perp}) \cdot \exp(-2\int (\alpha_m + \alpha_p) \cdot dz), \tag{S1}$$

$$B_C^{\parallel} = (\beta_m^{\parallel} + \beta_p^{\parallel}) \cdot \exp(-2\int (\alpha_m + \alpha_p) \cdot dz), \tag{S2}$$

$$B_M^{\parallel} = T_m \cdot \beta_m^{\parallel} \cdot \exp(-2\int (\alpha_m + \alpha_p) \cdot dz), \tag{S3}$$

where, $\beta_m$ and $\beta_p$ stand for the backscattering coefficients of atmospheric molecules and particles (i.e., aerosols or clouds), respectively; the superscript " $\perp$ " and " $\parallel$ " denote perpendicular-polarized and parallel-polarized components, respectively; $\alpha_m$ and $\alpha_p$ are the extinction coefficients of atmospheric molecules and particles, respectively. With these measured signals, the backscattering coefficients and extinction coefficients along with the depolarization ratio can be retrieved. The particle backscattering coefficient can be obtained as

2

$$\beta_p = \beta_m \left[ T_m \frac{1+\delta}{1+\delta_m} \frac{B_C^{\parallel}}{B_M^{\parallel}} - 1 \right], \tag{S4}$$

where, $\delta_m$ is the depolarization ratio of atmospheric molecules. $\delta$ is the volume depolarization ratio, which can be directly derived from the ratio of perpendicular channel and parallel channel:

$$\delta = B_C^{\perp} / B_C^{\parallel}. \tag{S5}$$

Note that the polarizing/depolarizing effect and polarization cross-talk of optical components would also affect the measurements of the depolarization ratio, which need to be carefully corrected and calibrated (4-7). The particle extinction coefficient can be delivered from the molecular channel only.

$$\alpha_p = -\frac{1}{2} \frac{\partial}{\partial z} \ln(\frac{B_M^{\parallel}}{\beta_m^{\parallel}}) - \alpha_m. \tag{S6}$$

Note that Eq. (S6) is applicable to the aerosol extinction and would underestimate the cloud extinction due to strong multiple scattering effect. The cloud extinction corrected from multiple scattering effect should be retrieved by an iterative process, as detailed in the main text. Furthermore, considering that our retrieval algorithm of microphysical properties is mainly aimed at water clouds, it is essential to identify the thermodynamic phase of the clouds before applying the retrieval of microphysical properties. The particle depolarization ratio from lidar measurements contributes to identifying the phase of the clouds because ice crystals usually induce a stronger depolarization than water droplets do by means of multiple scattering. Thus, each bin of profiles can be classified into four types in this study: aerosols, water clouds, ice clouds, and NaN (i.e., clear sky region or invalid data). In final the water cloud layer excluded from aerosols and ice clouds is selected and the water cloud properties are retrieved, e.g., cloud extinction ($\alpha_c$), cloud droplet effective radius ($r_{eff}$), cloud droplet number concentration ($N_d$), liquid water content (LWC), etc.

## S3. The relationships between cloud droplet number concentration ($N_d$) and liquid water content (LWC) along with cloud extinction ($\alpha_c$) and cloud droplet effective radius ($r_{eff}$)

The water clouds generally compose of liquid droplets, which are almost spherical shape. The cloud droplet number concentration ($N_d$) can be expressed as:

$$N_d = \int_0^{\infty} n(r) \mathrm{d}r, \tag{S7}$$

where $n(r)$ is the number size distribution of droplets. The mean surface droplet radius ($r_s$), the mean volume droplet radius ($r_v$) and the cloud droplet effective radius ($r_{eff}$) can be calculated by

$$r_s^2 = \frac{\int_0^{\infty} r^2 n(r) \mathrm{d}r}{\int_0^{\infty} n(r) \mathrm{d}r} = \frac{\langle r^2 \rangle}{N_d}, \tag{S8}$$

$$r_v^3 = \frac{\int_0^{\infty} r^3 n(r) \mathrm{d}r}{\int_0^{\infty} n(r) \mathrm{d}r} = \frac{\langle r^3 \rangle}{N_d}, \tag{S9}$$

$$r_e = \frac{\int_0^{\infty} r^3 n(r) \mathrm{d}r}{\int_0^{\infty} r^2 n(r) \mathrm{d}r} = \frac{\langle r^3 \rangle}{\langle r^2 \rangle}, \tag{S10}$$

where the symbol $\langle \cdot \rangle$ means the average operator. The $k$ coefficient is defined as the ratio between the cubic power of the mean volume droplet radius and the cubic power of the effective radius.

Also, it can be proved that $k$ coefficient is equal with the ratio between the square power of the mean surface droplet radius and the square power of the effective radius.

$$k = \frac{r_v^3}{r_e^3} = \frac{r_s^2}{r_e^2} = \frac{\langle r^2 \rangle^3}{N_d \langle r^3 \rangle^2}. \tag{S11}$$

Extensive publications set up the database of $k$ coefficient from various *in situ* measurements of typical cloud scenarios, in which $k$ coefficient varies greatly (8-11). Here, we assume that $k$ coefficient is stable within a single cloud layer as they are only dependent on the shape of the droplet size distribution. The cloud extinction ($\alpha_c$) can be expressed as (12)

$$\alpha_c = \int_0^\infty Q_{ext} n(r) \pi r^2 \mathrm{d}r, \tag{S12}$$

where $Q_{ext}$ is the extinction efficiency. Given that the size of the particles (cloud droplets are larger than 5 µm in general) is far greater than the wavelength of transmitter (532 nm in this case), it is a well-known fact that the extinction efficiency can be regarded as nearly constant (see in *SI* Fig. S8) (12)

$$Q_{ext} \approx 2. \tag{S13}$$

Thus, Eq. (S7) can be rewritten as

$$\alpha_c = \langle Q_{ext} \rangle \int_0^\infty n(r) \pi r^2 \mathrm{d}r = \langle Q_{ext} \rangle N_d \pi r_s^2. \tag{S14}$$

Using Eq. (S6) and (S8), $N_d$ could be reformulated as

$$N_d = \frac{\alpha_c}{\langle Q_{ext} \rangle \pi r_s^2} = \frac{\alpha_c}{\langle Q_{ext} \rangle \pi k r_e^2} \propto \alpha_c r_e^{-2}. \tag{S15}$$

As for the liquid water content (LWC), it is given by

$$\text{LWC} = N_d \rho_w \frac{4}{3} \pi r_v^3, \tag{S16}$$

where $\rho_w$ is the water density. Using Eq. (S5), (S9) and (S10), LWC can be rewritten as

$$\text{LWC} = \frac{\alpha_c \rho_w \frac{4}{3} r_v^3}{\langle Q_{ext} \rangle k r_e^2} = \frac{2}{3} \rho_w \alpha_c r_e. \tag{S17}$$

To describe the relative change of the cloud properties with the aerosol loading, the ACI parameters are adopted here. Then the ACI parameters can be estimated as

$$\text{ACI}_N = \frac{\mathrm{d} \ln N_d}{\mathrm{d} \ln \alpha_a} = \frac{\mathrm{d} \ln \alpha_c r_e^{-2}}{\mathrm{d} \ln \alpha_a}, \tag{S18}$$

$$\text{ACI}_R = -\frac{d \ln r_e}{d \ln \alpha_a}, \tag{S19}$$

$$\text{ACI}_L = -\frac{d \ln \text{LWP}}{d \ln \alpha_a} = -\frac{d \ln \int \text{LWC} \cdot dz}{d \ln \alpha_a}, \tag{S20}$$

where $\alpha_a$ is the aerosol extinction below the water cloud. Note that ACI$_N$ can be calculated through this way only if the values of $\alpha_c$ and $r_{eff}$ are from the same cloud layer. Otherwise, the assumptions

of a stable $k$ value may not be tenable as different cloud samples might yield various cloud droplet distributions (11).

**S4. Investigation of signal sensitivities and the optimization of lidar configuration**

The size of the dual FOVs is crucial for retrieving cloud properties, thus the configuration needs to be optimized before measuring. To guarantee the robustness of the cloud products, in other words, the optimization of the dual FOVs, is to make the attenuated backscattering signals from two molecular channels sensitive to $\alpha_c$ and $r_e$, respectively. Because all cloud products are related to the retrievals of $\alpha_c$ and $r_e$ (see *SI* Text S3). The sensitivities of $\alpha_c$ and $r_e$ to the molecular signals are defined as:

$$SC_{\alpha_c}(z) = \frac{\alpha_c(z)}{\beta'_{S1}(z)} \frac{\partial \beta'_{S1}(z)}{\partial \alpha_c(z)}, \tag{S21}$$

$$SC_{r_e}(z, z') = \frac{r_e(z)}{\beta'_{S2}(z)} \frac{\partial \beta'_{S2}(z)}{\partial r_e(z)}, \tag{S22}$$

where $\beta'_{S1}(z)$ and $\beta'_{S2}(z)$ are the attenuated backscattering signals from two molecular channels with different receiver FOVs; subscript 1 denotes the narrow FOV$_1$, and subscript 2 represents the wide FOV$_2$, respectively.

Here we focus our study on low-level water clouds, which might be adjacent to the boundary layer, and which are more likely to strongly interact with high concentrations of aerosols from pollution. Moreover, the intensified aerosol-cloud interaction may lead to the deviation of cloud profile from the adiabatic assumption. This assumption could be close to the real situation for high-level convective clouds, but is not reliable for low-level water clouds with small cloud droplets. Hence, in this study, we aim to optimize the lidar configuration with the cloud-base height of 2 km, the cloud thickness of 200 m, and the $r_e$ value of 6 μm. The optimization for other cloud scenarios can be performed with the same strategy, and therefore is not repeated here.

As in *SI* Fig. S10(a), the sensitivities of wide FOV$_2$ molecular channel to $r_e$ with different cloud optical depth are presented. The variable of the abscissa axis is defined as

$$x = \frac{\rho \cdot \mathrm{FOV}_2 / 2 \cdot (z + H)}{z}, \tag{S23}$$

where $\rho$ is the effective dimensionless droplet radius (13); $z$ denotes the cloud thickness; $H$ represents the cloud-base height. Based on different cloud optical depth, the wide FOV$_2$ (full width) is optimized to be 2.0 mrad (full width), of which signal sensitivity is close to maximum ($x = 0.8$). Note that the optimal FOV$_2$ would shift corresponding to cloud-base height and cloud thickness. Basically, the thicker the cloud thickness is, the larger the optimal FOV$_2$ will be. The situation is reversed for the cloud-base height. If we specify $r_e$ as 6 μm ($\rho = 70.8$ for 532 nm) and $x = 0.8$, the relationship between the optimal FOV$_2$, cloud-base height $H$, and cloud thickness $z$ can be simplified as:

$$\mathrm{FOV}_2 \approx \frac{0.02H}{z} \text{ (for } H \gg z). \tag{S24}$$

The optimization of narrow FOV$_1$ would be more complicated. As depicted in *SI* Fig. S10(b), the sensitivities of molecular signals to $\alpha_c$ monotonically decrease as $x$ (in proportion to FOV$_1$) increase, no matter how the conditions change. In theory, the smaller the FOV$_1$ is, the higher the sensitivity will be. However, the FOV$_1$ cannot be narrowed down without restriction due to practical limitations. The overlap function (i.e., the incomplete geometrical overlap of the receiver FOV and the laser beam, varying from 0 to 1) is very crucial for any lidar when measuring

attenuated backscattering signals, as the overlap function must be corrected within the incomplete overlap region (i.e., overlap function<1). However, to the best of our knowledge, there are very few (if any) methods to correct and quantify the overlap function with quality accuracy. The error of quantifying the overlap function is detrimental to the retrieval. Thus, in this work, we choose to enlarge the $FOV_1$ properly to prevent measuring low-level clouds within the incomplete overlap region, without losing too much signal sensitivity at the same time. As result, the $FOV_1$ is set to 1 mard (full width), ensuring that the narrow $FOV_1$ molecular channel can directly measure signals above 1.5 km (typical urban boundary layer height) without correcting the overlap function. The incomplete overlap region of the narrow $FOV_1$ channel is estimated by the ratio between the signals of the narrow $FOV_1$ channel and the wide $FOV_2$ channel in the cloud-free days. Namely, the ratio between the two signals should be very steady above 1.5 km if the lidar system was tuned well.

## S5. Determination of resolutions in practical cases

The dual-FOV HSRL technique can easily achieve very high original resolutions with sufficient SNR when measuring molecular attenuated backscattering signals, which should mainly benefit from the relatively large scattering cross section of Rayleigh scattering (12). However, the accuracy of the cloud products with extremely high vertical resolution might be degraded due to the nature of the under-determined inversion (13, 14). The high temporal or vertical resolution also raises a potential risk for retrieving cloud products due to insufficient SNR. Basically, the higher the resolutions are, the less accurate the retrieval might be. However, one thing we cannot ignore is the low resolutions also lead to unreliable retrieval of the cloud products. The cloud-free region would be averaged at the cloud edges (i.e., corresponding to unrealistic low $r_e$ and LWC values), which significantly declines signal sensitivities (see *SI* Text S4). Thus, it is rather challenging to determine what resolutions are most appropriate theoretically, since the explanation for differences may involve several complicated factors, e.g., different lidar configurations, the practical cloud scenarios, the way to solve the under-determined problem, etc.

Thus, we recommend performing the retrieval process as a tradeoff between resolution and accuracy in practical cases: the retrieval can be performed multiple times with different vertical resolutions, which is directly proportional to the original resolutions of signals (e.g., 15 m, 22.5 m, etc. for original vertical resolution of 7.5 m; the determination of temporal resolution can be performed with similar strategy). Then the highest available resolutions can be assessed by identifying the results that were not significantly degraded.

Moreover, *SI* Fig. S11 illustrates how this strategy works in a specific example of $r_e$ and LWC results, corresponding to a thin water cloud. As can be seen in *SI* Fig. S11(a), even for such a high vertical resolution of 7.5 m and temporal resolution of 5 min, we can still obtain the cloud products with reasonable accuracy (for instance, within ±10% deviation in this case, compared to the 15-m and 10-min results). However, the 7.5-m and 2-min results have substantial biases (exceed ±20% deviation in this case), shown in *SI* Fig. S11(b). Thus we choose not to use this result in further analysis. The temporal resolution can be improved if we could employ a more powerful or higher repetition rate single-mode laser, which is feasible for future work. However, it is noteworthy that very high vertical resolutions (for instance, employing a data acquisition system with very high sampling rate of up to hundreds of megahertz) should not be considered as a feasible resolution for the cloud products, because the high-speed acquisition system does not increase SNR.

6

**S6. Investigation of retrieval susceptibilities to different factors**

To fully evaluate the performance of this technique, factors relevant to the retrieval are tested for whether they have significant effects on the results through simulations. The basic parameters for these simulations are referred in *SI* Table S2. One of these parameters might be changed, depending on the relevant factors we study. Since the signal sensitivity of $\alpha_c$ is much higher than that of $r_e$, the performance of the $r_e$ retrieval is used as an indicator in the following discussion for the sake of simplicity.

(1) *Cloud-base heights*. We present the statistical results of true values and retrieved values with the parameters depicted in *SI* Table S2 (homogenous cloud) but different cloud-base height (e.g., 4 km, above which usually are mixed-phase cloud or ice cloud) in *SI* Fig. S12(a). In theory, the sensitivity of the attenuated backscattering molecular signal would decrease as the cloud-base height increases compared to the optimal cloud-base height; note that the lidar configuration is mainly designed for the low-level water clouds (see *SI* Text S4). Thus the performance with the set configuration slightly degrades. The in-depth reason for such a degradation is that, with other conditions unchanged, the higher cloud-base height is, the smaller cloud droplet radius with the maximum signal sensitivity will be. Since the optimal cloud droplet radius shifts from 6 μm (see *SI* Text S4) to a smaller value, the degradation of the retrieval is logical. But the retrieval uncertainty generally falls within acceptable levels, which suggests that the signal sensitivity as a function of the cloud-baes height is smooth enough in the vicinity of its maximum (2 km in this case) within the typical height ranges of water clouds.

(2) *Initialization with different constant values.* Our recommendation about the initialization of the retrieval has been detailed in *Materials and Method* of the main text, and hence is not repeated here. However, how an initialization with different constant values affects the retrieval is described. The statistical comparison of true values and retrieved values with the same parameters but different constant initialization (e.g., $r_{e, int}$ = 12 μm) is presented in *SI* Fig. S11(b). Compared to Fig. 2(A), we found no substantial difference. Subsequently, an initialization with different constant values does not impose a significantly higher uncertainty on the final results from our investigations, which suggests that the cost function does not have multiple local minimums in the parameter space in general. The indiscernible differences could be partially accounting for the stochastic nature in the MC simulations.

(3) *Initialization with the adiabatic profile*. The effect of initialization with the adiabatic condition would be considered as follows: the *a priori* assumption of the retrieval is an adiabatic condition (i.e., the linear increasing LWC and the constant $N_d$), but the simulated true profile is a homogenous condition. The adiabatic profiles of $N_d$ and LWC could be expressed:

$$N_d(z) = \begin{cases} N_0, & z \geq z_b \\ 0, & z < z_b \end{cases} \tag{S25}$$

$$\text{LWC}(z) = \begin{cases} k(z - z_b), & z \geq z_b \\ 0, & z < z_b \end{cases} \tag{S26}$$

where $z_b$ is the cloud-base height; $k$ is the slope of linear increasing LWC. Using Eq. (S15), (S17), (S25) and (S26), the relationship between $r_e$ and $z$ could be found:

$$\frac{\text{LWC}(z)}{\text{LWC}(z_{ref})} = \frac{k(z - z_b)}{k(z_{ref} - z_b)} = \frac{\frac{2}{3}\rho_w \alpha_c(z) r_e^{-2}(z) \cdot r_e^3(z)}{\frac{2}{3}\rho_w \alpha_c(z_{ref}) r_e^{-2}(z_{ref}) \cdot r_e^3(z_{ref})} = \frac{N_d(z) \cdot r_e^3(z)}{N_d(z_{ref}) \cdot r_e^3(z_{ref})}$$ (S27)

$$\Rightarrow \left. r_e(z) \middle/ r_e(z_{ref}) \right. = \left( \left. z - z_b \middle/ z_{ref} - z_b \right. \right)^{1/3},$$

where $z_{ref}$ is an arbitrary reference height. Once the $r_e(z_{ref})$ is fixed (e.g., $r_e(z_{100\,m}) = 12\ \mu m$), the range-resolved profile of $r_e$ can be computed. The statistical results with respect to true values and retrieved values are shown in *SI* Fig. S11(c). As the figure shows, the retrievals do not exhibit significant disparity compared to Fig. 2(A). The reason for this pattern is similar to that of the initialization with different constant values.

In conclusion, with the optimized lidar configuration as detailed in *SI* Text S4, the different initializations would not impose a significantly higher uncertainty on the retrieval of the cloud products, which corroborates the robustness of this technique. The average performances with the higher cloud-base height are slightly degraded due to the decline in signal sensitivities.

**S7. A detailed explanation regarding the comparison between the cloud radar and the dual-FOV HSRL**

The related observations of the cloud radar, the dual-FOV HSRL and the high-resolution radiosonde are provided in *SI* Fig. S4. To prevent potential retrieval biases in the comparison, it is essential to identify the thermodynamic phase of clouds. The upper layer in *SI* Fig. S4(b-c) should be considered as water clouds due to the high backscattering coefficients and the low depolarization ratios. The steady depolarization ratios within the water clouds suggest the presence of ice crystals below the water clouds, which is a typical situation on the coexistence of supercooled liquid and ice layers due to the complex depolarization effect of ice crystals (also can refer the Phase 2 in Fig. 3) (2). A very similar depolarization pattern could be found in the measurements from winter mountain storms that contain supercooled clouds (15, 16). We propose that the transmitted linear polarized light might be changed into elliptic polarized light after penetrating the random oriented ice crystals to cause such a phenomenon. Given that the depolarization ratios are lower than typical values of ice crystals, those features below the water clouds might be formed by the mixing of ice crystals and droplets. The temperature profile measured from the high-resolution radiosonde (17) in the nearest meteorological station (39.80° N, 116.47° E) shown in *SI* Fig. S4(d) also supports the presence of supercooled clouds. The depolarization observations during 2:10-2:40 UTC+8 without a clear separation indicate that the cloud layer might be contaminated by ice crystals. The white lines denote the water cloud base, and the cloud layer contaminated by ice crystals likely is shaded by gray color in *SI* Fig. S4(b-c). It is noteworthy that the valid height ranges of retrieved microphysical properties are limited by the SNR of the wide-FOV channel, varying from 200 to 400 m above the water cloud base. The presented height ranges in *SI* Fig. S4(b-c) are wider than those of microphysical properties actually, because those figures are retrieved from the narrow-FOV receiver with larger diameter in comparison with the wide-FOV channel. Since the comparison aims to the pure water clouds, the retrievals of the cloud radar and the dual-FOV HSRL have been confined to the same height ranges. Those data points with potential mixed ice crystals and non-overlapping height ranges have been excluded.

**Figures and Tables**
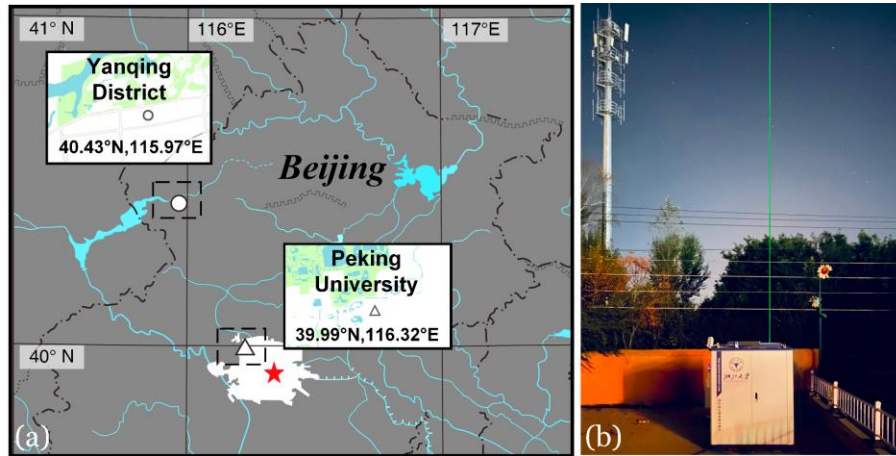


**Figure S1.** (**a**) The location of the field campaign. The triangular sign denotes the Peaking University site; the circle sign denotes the Yanqing site. (**b**) The appearance of the running dual-FOV HSRL system.
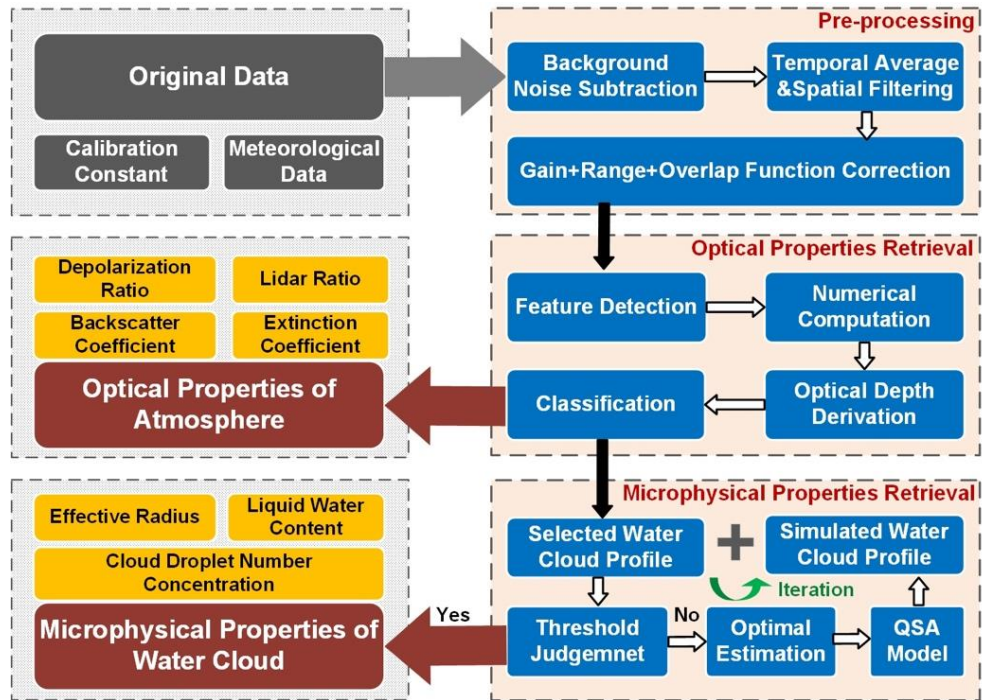
**Figure S2.** Lidar data processing scheme starting from raw data and calibrated data to products (properties of aerosols and clouds). The grey color cells indicate the raw data. The blue cells summarize the actions to be implemented for the data processing. The red color cells refer to the final products. The properties of aerosols and clouds are subdivided into detailed products (yellow).
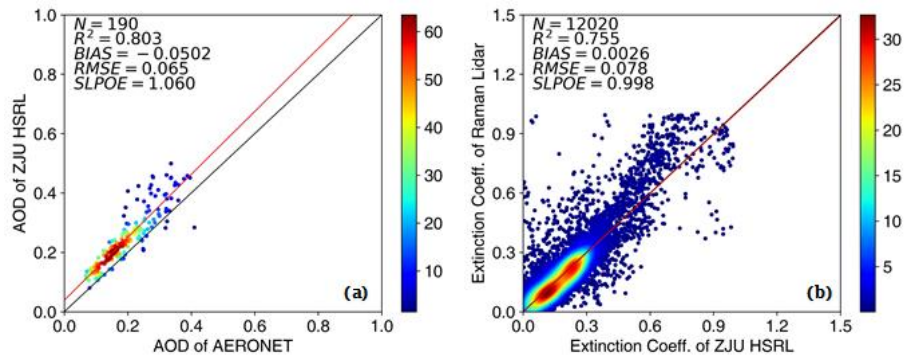
**Figure S3.** Correlation of aerosol optical properties obtained by the dual-FOV HSRL and other instruments. (**a**) Comparison of aerosol optical depth (AOD) between dual-FOV HSRL and sun photometer. (**b**) Comparison of extinction between dual-FOV HSRL and single-FOV Raman lidar.
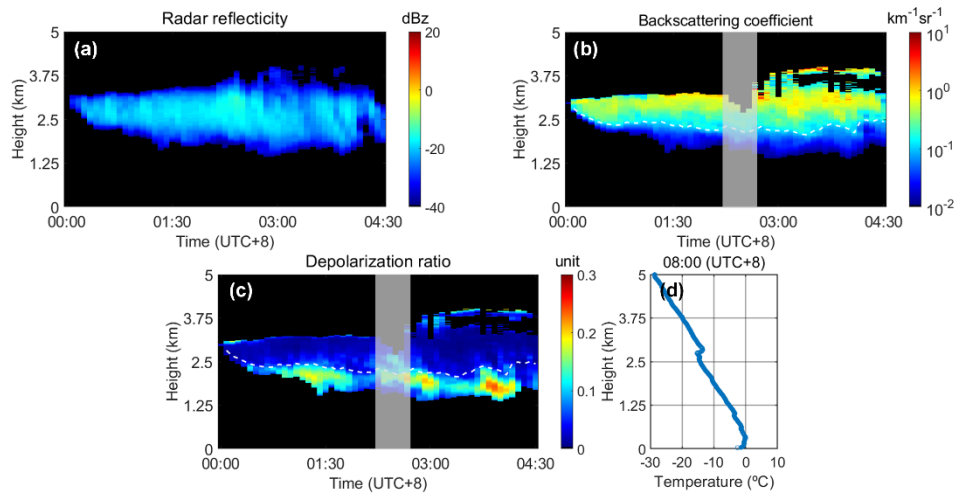
**Figure S4.** The coincident observations of the cloud radar, the dual-FOV HSRL and the high-resolution radiosonde on 06 December 2020 over the PKU site. (**a**) Radar reflectivity observed by the cloud radar. (**b-c**) Backscattering coefficient (b) and depolarization ratio (c) observed by the dual-FOV HSRL. The white lines denote the cloud base of the water clouds, and the shaded gray region is considered to be contaminated by the ice crystals. (**d**) The temperature profile measured from the high resolution radiosonde at 08:00 UTC+8.
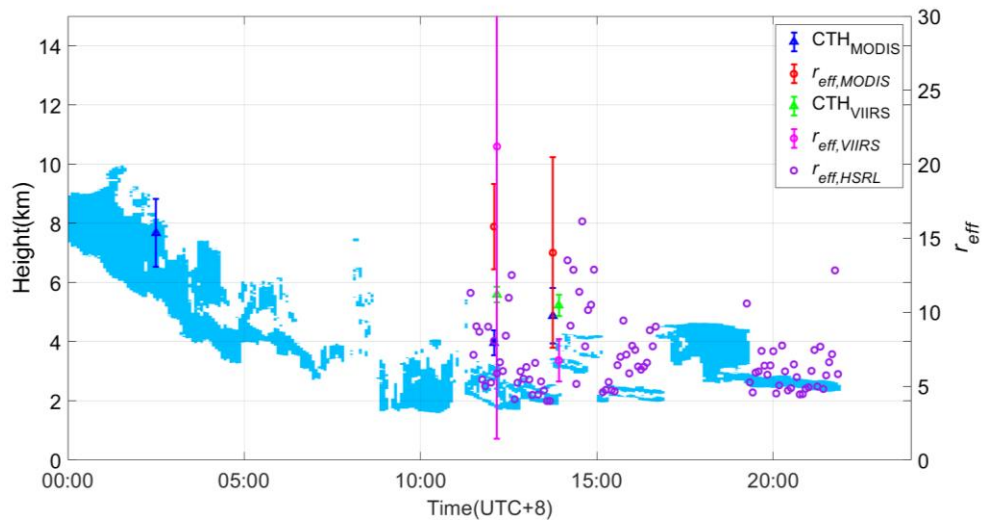
**Figure S5.** Comparison of satellite retrieved cloud properties with the dual-FOV HSRL observations, including cloud top height (CTH) and $r_{eff}$. The blue areas indicate the cloudy regions observed by the dual-FOV HSRL. However, the limited revisit time of the satellite hampers a further comparison between the dual-FOV HSRL and satellite.
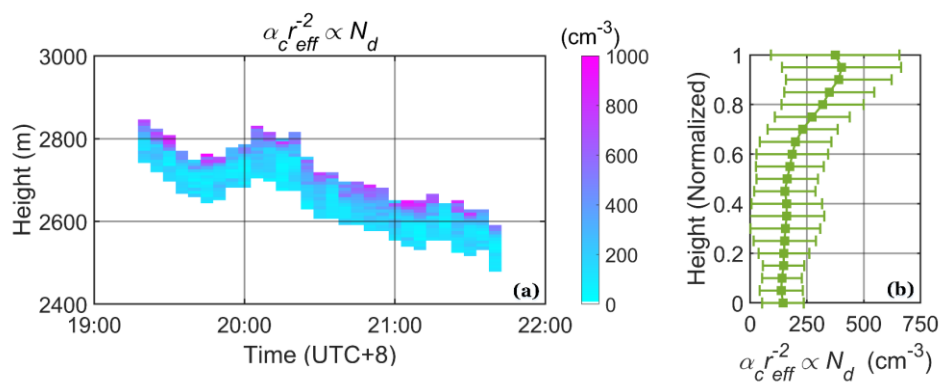
**Figure S6.** (**a**) Same as Fig. 5(a-b), but showing the estimations of $N_d$. (**b**) Same as Fig. 5(c-d), but showing the estimations of $N_d$.
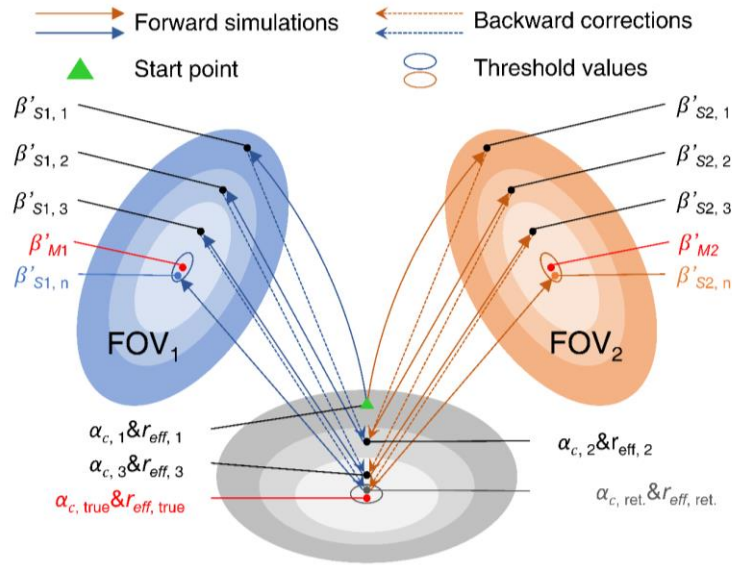
**Figure S7.** The illustration of the iterative optimal estimation method. The ellipses show the differences between the simulated signals with the measured signals (blue and orange) or the difference between the current $\alpha_c$ and $r_{eff}$ with the true $\alpha_{c,\ ture}$ and $r_{eff,\ true}$ (gray). The retrieval process starts with the forward simulations of $\beta'_{S1,\ 1}$ and $\beta'_{S2,\ 1}$ corresponding to the first initial values $\alpha_{c,\ 1}$ and $r_{eff,\ 1}$. The solutions for water cloud properties are generated to minimize the deviations of the simulated signals. This process would be repeated a few times until the differences between the simulated signals with the measured signals are below the thresholds.
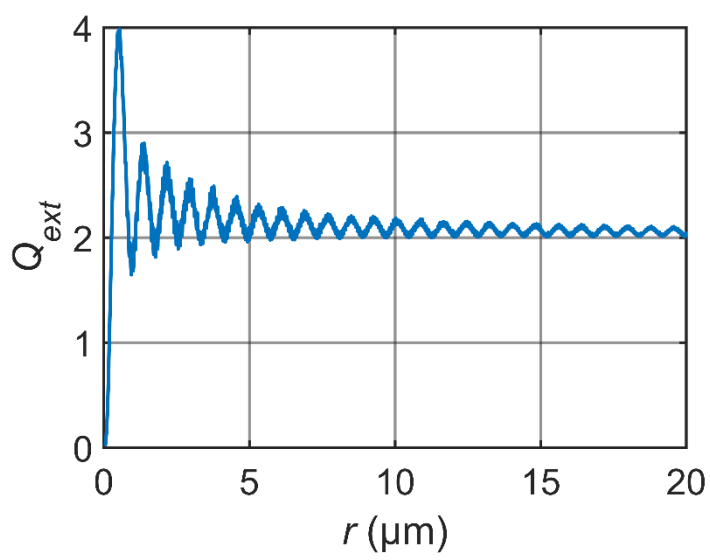
**Figure S8.** The extinction efficiency $Q_{ext}$ is nearly constant when the particle radius is far greater than the transmitter wavelength (532 nm in this case).
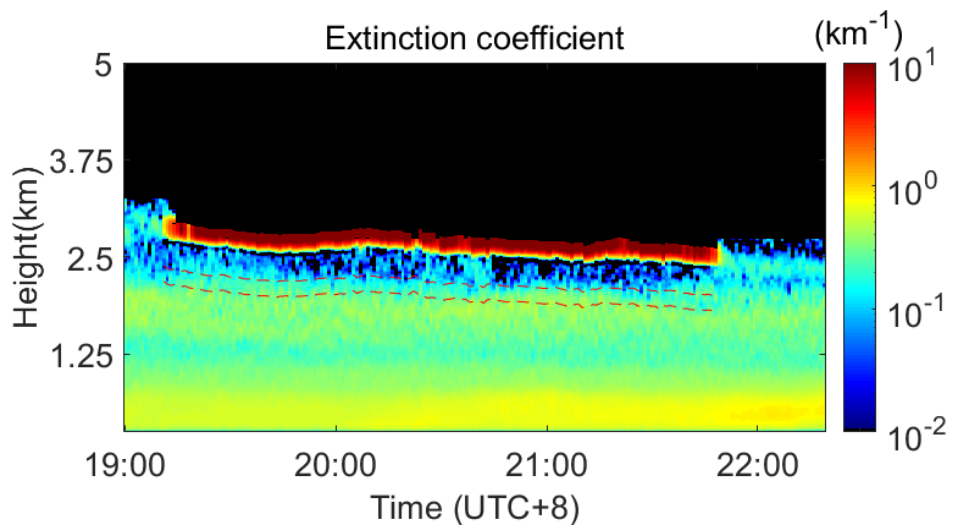
**Figure S9.** Extinction coefficient (multiple scattering affected) with resolution of 1 min and 7.5 m observed by the dual-FOV HSRL on 14 November 2020 over Beijing YQ site. The dash red lines denote the height range from 400 to 600 m below the cloud base.
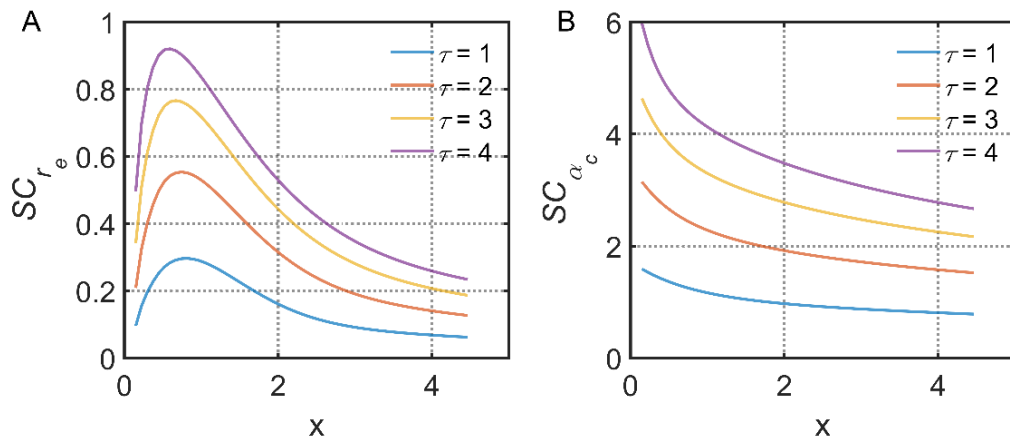
**Figure S10.** Signal sensitivities to(**a**) the effective radius  and (**b**) the cloud extinction  with different cloud optical depth ( $\tau$ ).
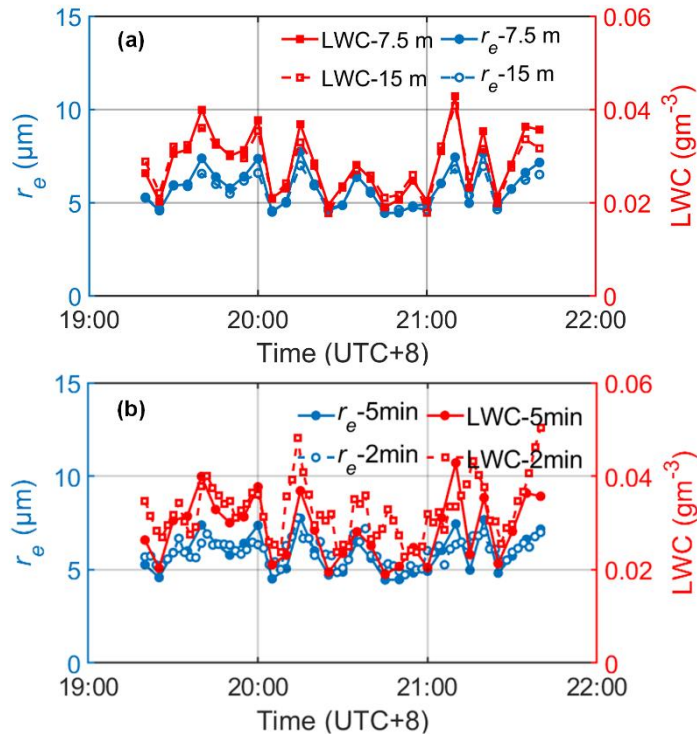
**Figure S11.** The comparisons of retrieved $r_e$ and LWC with different resolutions: (**a**) With the same 5 min temporal resolution, 7.5-m results and 15-m results are presented; (**b**) With the same 7.5 m vertical resolution, 5-min results and 2-min results are presented.
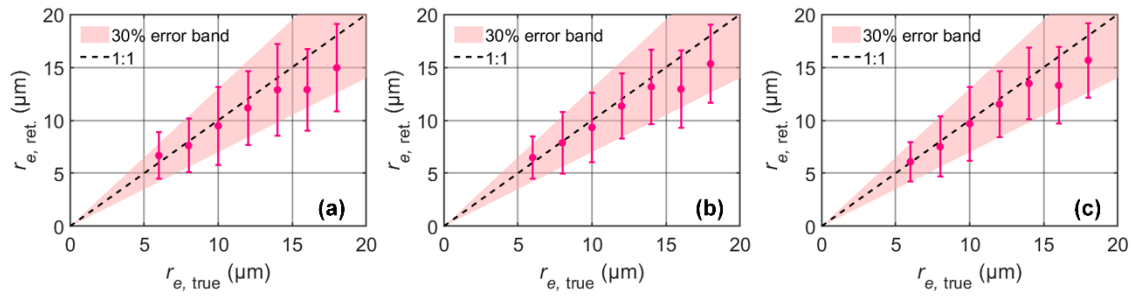
**Figure S12.** Same as Fig. 2(A), but with (**a**) different cloud-base height (4km), (**b**) initialization with different constant value ($r_{e, int}$ = 12 μm) and (**c**) initialization with adiabatic condition ($r_e(z_{100 m})$ = 12 μm).

**Table S1.** Specifications of ZJU dual-FOV HSRL system.

| Specifications | Value |
|---|---|
| *Transmitter* | |
| Manufacturer of laser | Continuum, Inc. |
| Type of pulsed laser | Injection Seeded Nd:YAG laser |
| Type of seed laser | DBR laser |
| Repetition (Hz) | 10 |
| Laser wavelength (nm) | 532 |
| Laser energy (mJ) | 100 |
| Pulse width (ns) | 10 |
| Linear polarization purity | >10000:1 |
| Beam diameter (mm) | 30 |
| *Receiver* | |
| Manufacturer of narrow-FOV telescope | CELESTRON, Inc. |
| Type of narrow-FOV telescope | Schmidt-Cassegrain |
| Diameter of narrow-FOV telescope (mm) | 280 |
| FOV of narrow-FOV telescope (mrad) | 0.36-1 (adjustable) |
| Manufacturer of wide-FOV telescope | Meade, Inc. |
| Type of wide-FOV telescope | Kepler |
| Diameter of wide-FOV receiver (mm) | 95 |
| FOV of wide-FOV receiver (mrad) | 2 |
| Interferometer filter bandpass (nm) | 0.3 |
| *Detector and DAQ* | |
| Manufacturer of detector | Hamamatsu |
| Type of detector | PMT, R7518 |
| Type of DAQ | Analog |
| Sampling rate of DAQ (MHz) | 20 |
| Sampling resolution (bits) | 16 |

**Table S2.** Parameters used in the MC simulations for Fig. 2(a) and (b). The diameter and divergence angle of the laser beam are regarded as ideally zero for the sake of simplicity. Combinations of different droplet sizes and single-scattering extinction were used to verify the algorithm and estimate the uncertainty of the retrieval under different cloud scenarios.

| Parameters | Value |
|---|---|
| *Lidar* | |
| Laser wavelength (nm) | 532 |
| Diameter of primary telescope (mm) | 280 |
| FOV of primary telescope (mrad) | 1 |
| Diameter of near-range receiver (mm) | 95 |
| FOV of near-range receiver (mrad) | 2 |
| Spatial resolution (m) | 7.5 |
| *Water cloud* | |
| Cloud height range (m) | 2010-2160 |
| Liquid water content (gm$^{-3}$) | 0.05-0.45 |
| Effective radius (µm) | 6-18 |

**Table S3.** Parameters used in the MC simulations for Fig. 2(d). Ground/Space represents the platform of the lidar (ground-based lidar or spaceborne lidar); Distance means the interval from the water cloud base to the lidar system. Optical depth and effective radius are the water cloud properties served as the basic inputs into the MC simulations.

| Case | Ground/Space | FOV (mrad) | Distance (km) | Optical depth | Effective radius (μm) |
|------|--------------|------------|---------------|---------------|-----------------------|
| 1 | Space | 1.3 | 700 | 20 | 4 |
| 2 | Space | 1.3 | 700 | 16 | 4 |
| 3 | Space | 1.3 | 700 | 12 | 4 |
| 4 | Space | 1.3 | 700 | 8 | 4 |
| 5 | Space | 1.3 | 700 | 4 | 4 |
| 6 | Space | 0.13 | 700 | 20 | 4 |
| 7 | Ground | 6 | 2 | 8 | 8 |
| 8 | Ground | 0.5 | 1 | 8 | 12 |
| 9 | Ground | 2 | 0.7 | 6 | 10 |
| 10 | Ground | 1 | 1.5 | 5 | 10 |

**SI References**

1.  Hair JW*, et al.* (2008) Airborne High Spectral Resolution Lidar for profiling aerosol optical properties. *Applied Optics* 47(36):6734-6752.
2.  Wang N*, et al.* (2021) Development of ZJU High-spectral-resolution Lidar for Aerosol and Cloud: Feature Detection and Classification. *Journal of Quantitative Spectroscopy and Radiative Transfer* 261:107513.
3.  Liu D*, et al.* (2013) Retrieval and analysis of a polarized high-spectral-resolution lidar for profiling aerosol optical properties. *Opt. Express* 21(11):13084-13093.
4.  Luo J*, et al.* (2017) Polarization properties of receiving telescopes in atmospheric remote sensing polarization lidars. *Applied Optics* 56(24):6837-6845.
5.  Luo J*, et al.* (2017) Effects of a nonideal half-wave plate on the gain ratio calibration measurements in polarization lidars. *Applied Optics* 56(29):8100-8108.
6.  Luo J*, et al.* (2018) Rotating a half-wave plate by 45°: An ideal calibration method for the gain ratio in polarization lidars. *Optics Communications* 407:361-366.
7.  Freudenthaler V (2016) About the effects of polarising optics on lidar signals and the Δ90 calibration. *Atmos. Meas. Tech.* 9(9):4181-4255.
8.  Martin G, Johnson D, & Spice A (1994) The Measurement and Parameterization of Effective Radius of Droplets in Warm Stratocumulus Clouds. *Journal of Atmospheric Sciences* 51:1823-1842.
9.  Miles N, Verlinde J, & Clothiaux E (2000) Cloud Droplet Size Distributions in Low-Level Stratiform Clouds. *Journal of the Atmospheric Sciences* 57:295-311.
10. Lu M-L & Seinfeld JH (2006) Effect of aerosol number concentration on cloud droplet dispersion: A large-eddy simulation study and implications for aerosol indirect forcing. 111(D2).
11. Brenguier JL, Burnet F, & Geoffroy O (2011) Cloud optical thickness and liquid water path – does the k coefficient vary with droplet concentration? *Atmos. Chem. Phys.* 11(18):9771-9786.
12. Bohren C & Huffman D (1983) *Absorption and scattering of light by small particles*.
13. Malinka AV & Zege EP (2007) Possibilities of warm cloud microstructure profiling with multiple-field-of-view Raman lidar. *Applied Optics* 46(35):8419-8427.
14. Schmidt J*, et al.* (2014) Dual-FOV Raman and Doppler lidar studies of aerosol—cloud interactions: Simultaneous profiling of aerosols, warm—cloud properties, and vertical wind. *Journal of Geophysical Research: Atmospheres* 119.
15. Sassen K, Zhao H, & Dodd GC (1992) Simulated polarization diversity lidar returns from water and precipitating mixed phase clouds. *Applied Optics* 31(15):2914-2923.
16. Sassen K (1991) The Polarization Lidar Technique for Cloud Research: A Review and Current Assessment. *Bulletin of the American Meteorological Society* 72(12):1848-1866.
17. Guo J*, et al.* (2021) Investigation of near-global daytime boundary layer height using high-resolution radiosondes: first results and comparison with ERA5, MERRA-2, JRA-55, and NCEP-2 reanalyses. *Atmos. Chem. Phys.* 21(22):17079-17097.